

RESEARCH ARTICLE

Electronic structure, thermomechanical and phonon properties of inverse perovskite oxide (Na₃OCl): An ab initio study

Shakeel Ahmad Khandy¹  | Ishtihadah Islam² | Amel Laref³ | Mathias Gogolin^{4,5} | Aurangzeb K. Hafiz⁶ | Azher M. Siddiqui²

¹Department of Physics, National Taiwan University, Taipei, Taiwan

²Department of Physics, Jamia Milia Islamia, New Delhi, India

³Department of Physics, College of Science, King Saud University, Riyadh, Saudi Arabia

⁴Institute of Inorganic Chemistry and Crystallography, University of Bremen, Bremen, Germany

⁵MAPEX Center for Materials and Processes, University of Bremen, Bremen, Germany

⁶Centre for Nanoscience and Technology, Jamia Milia Islamia, New Delhi, India

Correspondence

Shakeel A. Khandy, Department of Physics, National Taiwan University, Taipei 10617, Taiwan.
Email: shakeelkhandy11@gmail.com, shakeel11@phys.ntu.edu.tw

Funding information

King Saud University; University of Bremen

Summary

Within first principles calculations, the electronic structure, thermodynamic, mechanical stability, magnetism, and phonon properties of the inverse perovskite (Na₃OCl) have been summed up. The Birch-Murnaghan derived lattice constant and bond-lengths are identical, when compared to the experimental data. A direct energy gap of 2.18 eV observed from the band structure reveals the semiconducting nature of the present oxide. Also, the application of strain on electronic properties predicts the decrease in bandgap with respect to compressive strain and vice versa. The constituent nonmagnetic atoms in its crystal propose the total magnetic moment to be zero and the same is supported by susceptibility data. In addition to the negative Cauchy's pressure, the small bulk modulus compared to Young's modulus determined from elastic constants, possibly claims it as a brittle material. Also, the temperature dependent Gruneisen parameter (1.58) and Debye temperature (382.27 K) are determined to reveal the lattice thermal conductivity ($\kappa = 6.48$ W/mK) at room temperature.

KEYWORDS

electronic structure, mechanical strength, phonon properties, structural properties, thermal conductivity

1 | INTRODUCTION

Perovskites have long been an interesting topic for the researchers worldwide. The possible alterations in their transport and charge distributions, electronic structure, spin coupling, etc., have fueled their exploration and therefore endorse multifaceted and technological properties like half-metallicity (for spintronics), Piezoelectricity (for piezoelectric devices), ferromagnetism (for magnetism), magnetoresistance (for memory devices), high thermopower (for thermoelectrics), photovoltaic effect (for solar cells), high electrical conductivity (for electrode materials), etc.¹⁻³

Ideally, the perovskite compounds of ABO₃ kind crystallize in a cubic phase and follow the symmetry of space group Pm-3 m, where A cations occupy the eight corners, B cation is at body center, and the oxygen anions are located at six face centers of a cube. This family consists of vast number of compounds and is still being studied continuously for the electronic, magneto-electronic, and structural properties.^{6,7} Anti-perovskite (APV) compounds differ from normal perovskites only in the occupation of their face centers by metal cations instead of oxygen atoms/anions in the latter case. Magnetic or non-magnetic APVs display many fascinating physical

properties and new ones are predicted constantly. ACNi₃ (A = Mg, Zn, and Cd) compounds are reported by first-principles calculations as metallic in nature.⁸ More recently, novel cubic APVs of M₃XZ (M = Cr, Mn, Fe, Co, and Ni; Z = C, N; and X is one of the elements from Li to Bi) kind were screened to validate their stability and possible synthesis.⁹ The unique physical properties of such type of materials include nearly zero temperature resistance coefficient,¹⁰ high ionic conductivities,¹¹ negative thermal expansion,¹² which label them as promising materials for technological applications. Specifically, among alkali-based metal oxyhalides (Li₃OCl, Na₃OCl, Li₃OBr, and Na₃OBr) have established the superionic conductivity.¹³ Na₃OBr has been experimentally designated as soft material with bulk modulus of 58.6 GPa and theoretically a direct band gap superionic semi-conductor.^{14,15} Another member of this family, Na₃OCl crystallizes in a cubic structure with an experimental lattice constant of 4.50 Å and undergoes phase transition instantly.^{16,17} Recently, Pham et al discussed the phase transition and phonon dynamics of this compound.¹⁸ To the best of our knowledge, the electronic structure, thermal properties, magnetic interactions and mechanical aspects of cubic phase of this material (either theoretically or experimentally) are yet to be explored in detail. Hence, in a very first attempt, we tried to manifest the basic understandings of undecided structural, electronic bandgap, thermal conductivity, and mechanical properties of Na₃OCl oxide in this article. First, we focus on its electronic properties and effect of uniform strain on its band gap. Then, the elastic and mechanical properties accompanied by thermal coefficients are decided. Finally, we focus on phonon dynamics and lattice thermal conductivity of this material and its variation w.r.t. temperature.

2 | COMPUTATIONAL DETAILS

Density functional theory (DFT) has become the cost-effective, timeless and appreciable tool to pronounce the ground state properties of such materials, where the critical-phase transitions occur at low temperatures.^{9,15,18} Here, we simulate the Na₃OCl antiperovskite within the sophisticated Full potential Linearized Augmented Plane wave (FPLAPW) method¹⁹ implemented in Wien2K.²⁰ The structure is fully relaxed and optimized to achieve its stable ground state parameters via Birch Murnaghan's equation of state.

$$P(V) = \frac{3B_0}{2} \left[\left(\frac{V_0}{V} \right)^{7/3} - \left(\frac{V_0}{V} \right)^{5/3} \right] \left\{ 1 + \frac{3}{4} (B'_0 - 4) \left[\left(\frac{V_0}{V} \right)^{2/3} - 1 \right] \right\} \quad (1)$$

which is then expanded in series to get the internal energy as below,

$$E(V) = E_0 + \frac{9V_0B_0}{16} \left\{ \left[\left(\frac{V_0}{V} \right)^{2/3} - 1 \right]^3 B'_0 + \left[\left(\frac{V_0}{V} \right)^{2/3} - 1 \right]^2 6 - 4 \left[\left(\frac{V_0}{V} \right)^{2/3} - 1 \right] \right\} \quad (2)$$

where P , V_0 , V are the pressure, the reference volume and the deformed volume, B_0 and B'_0 is the bulk modulus and its derivative w.r.t. pressure. $E(V)$ represents the internal energy and E_0 the ground state energy of the system.

For exchange correlation, Perdew-Burke-Ernzerhof (PBE) parameterized correlation exchange-functional within generalized gradient approximation (GGA) is used.²¹ Following the Monkhorst and Pack convention, $10 \times 10 \times 10$ k -points are used for the Brillouin zone integrations and the (R_{MT}K_{Max}) cut-off is chosen as 7 to restrict the plane-wave number. The muffin tin radius (RMT) values are adjusted in a way to avoid charge leakage into the interstitial region. The energy convergence is set to 10^{-4} Ry while the charge convergence between two successive steps is constrained to 10^{-4} /a.u.³ or lesser than this. The optimization of the relaxed structure is first achieved by PBE-GGA method and the same relaxed structure is used to calculate the elastic parameters by using the cubic elastic code.^{22,23} To determine the variation of Debye temperature and Gruneisen parameter w.r.t. temperature, Gibbs2 code²³ is used. In this method the Gibbs function (G^*) is solved within quasi-harmonic Debye approximation and expressed as^{24,25},

$$G^*(V, P, T) = E(V) + P(V) + F_{\text{vib}}(\theta_D(V); T) \quad (3)$$

where $F_{\text{vib}}(\theta_D(V); T) = NK_B T \left[\frac{9\theta_D}{8T} + 3 \ln(1 - e^{-\theta_D/T}) - D\left(\frac{\theta_D}{T}\right) \right]$ is the vibrational term, $E(V)$ the total energy, $P(V)$ the hydrostatic pressure, $\theta_D(V)$ the Debye temperature, $D\left(\frac{\theta_D}{T}\right)$ the Debye integral, N the number of atoms per formula unit, k_B the Boltzmann's constant, respectively. Also, the Debye temperature $\theta_D = \frac{h}{k_B} (6 \pi^2 V^{1/2} N)^{1/3} f(v) \sqrt{\frac{B_S}{M}}$ is observed with the adiabatic bulk modulus $B_S = V \left(\frac{d^2 E(V)}{dV^2} \right)$ and M the molecular mass. Using different approximations, $G^*(V; P, T)$ is minimized w.r.t. V , as²⁵,

$$\left(\frac{dG^*(V; P, T)}{dV} \right)_{P, T} = 0 \quad (4)$$

While solving the above equation, heat capacity (C_V and C_P) at constant volume and pressure are obtained as below,

$$C_V = 3nk \left[4D \left(\frac{\theta_D}{T} \right) - \frac{3\theta_D/T}{e^{\theta_D/T} - 1} \right] \quad (5)$$

$C_P = C_V(1 + \gamma\alpha T)$ with $\gamma = \frac{d \ln \theta_D(V)}{d \ln V}$ and $\alpha = \gamma C_V / B_T V$ called as the Grüneisen parameter and thermal expansion, respectively.

While calculating the susceptibility data, we make use of Boltzmann transport theory implemented in BoltzTrap code²⁶ under the constant relaxation time and rigid band approximations.^{26,27} Finally, the phonon calculations are performed within the Quantum ESPRESSO^{28,29} software suite, using nonrelativistic PBEsol^{29,30} PAWs from the PS-library (version 0.1). The Monkhorst-Pack mesh and kinetic energy cut-off for the plane wave expansion is converged considering the pressure acting on the cell ($\Delta P < 0.06$ kBar) and the total energy ($\Delta E < 0.002$ eV). These considerations resulted in a 5x5x5 Monkhorst-Pack mesh and a kinetic energy cut-off of 1225 eV with a convergence-threshold of $1.36 \cdot 10^{-11}$ eV during the self-consistent step. Following this, the phonon frequencies were computed on a uniform $5 \times 5 \times 5$ q-point grid with an increased convergence-threshold of $1.36 \cdot 10^{-13}$ eV. The phonon dispersion is computed via Fourier-interpolation from the dynamic matrix. The above said optimized ground state structure is then utilized in computing the structural, electronic, and magnetic properties in detail.

3 | RESULTS AND DISCUSSION

3.1 | Structural properties

The relaxation of ground state structure is first achieved to extract the optimized lattice parameters of Na₃OCl compound with atomic coordinates; O (0,0,0), Cl (0.5,0.5,0.5), and Na (0,0.5,0.5). Here, the oxygen atom at the center of the cube with two unfilled *p*-states is bonded with the six sodium atoms occupying six faces of the crystal. The lattice volume is varied within the Birch-Murnaghan's procedure to calculate the ground state structural parameters. The variation of energy vs volume is shown in Figure 1 as well as the computed lattice parameters are presented in Table 1. The observed lattice constant as well as bond lengths from DFT calculations are in close agreement with the experimental data.^{16,17}

3.2 | Electronic properties

The optimized values are further used to calculate other physical properties, namely electronic structure, mechanical,

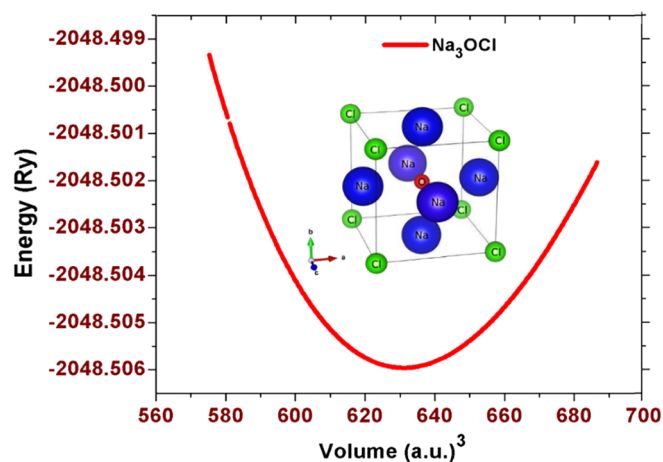


FIGURE 1 Volume-energy optimization plot for Na₃OCl inverse perovskite system [Color figure can be viewed at wileyonlinelibrary.com]

TABLE 1 Ground state structural parameters, lattice constant (a_0), derivative of Bulk modulus (B'), ground-state energy (E_0) and bond lengths (Na-Cl, Na-O and Cl-O) of Na₃OCl compound

Parameter	DFT	Expt.
a_0 (Å)	4.53	4.50, ¹⁶ 4.49 ¹⁷
V_0 (a.u)	631.08	—
B (GPa)	31.79	—
B'	5.95	—
E_0 (Ry)	-2048.506	—
Bond lengths (Å)		
Na-Cl	3.92	3.894 ¹⁷
Na-O	2.26	2.248 ¹⁷
Cl-O	3.20	3.179 ¹⁷

and thermal transport properties. Since, all the constituents of the system under study are nonmagnetic; therefore, the structural optimizations reveal the nonmagnetic configuration to be the most stable state. Then the band structure along the high symmetry Brillion zone (BZ) directions is firstly confirmed and displayed in Figure 2A. The absence of energy states at the fermi level (EF) directly confirms the insulating/semiconducting behavior of this material. As seen from the relaxed electronic structure, the valence band extents from -3.5 eV to 0.0 eV; while as the conduction band starts above the band gap. The valence band maximum (VBM) and minima of the conduction band (CBM) are restricted at the Γ -point of the BZ with a direct band gap of 2.18 eV; which is larger than the band gap of Na₃OBr (1.81 eV).¹⁵ The origin of increased band gap lies in the interaction of *p*-states of O and Cl in Na₃OCl, while as this interaction is weak in case of O and Br in case of Na₃OBr.

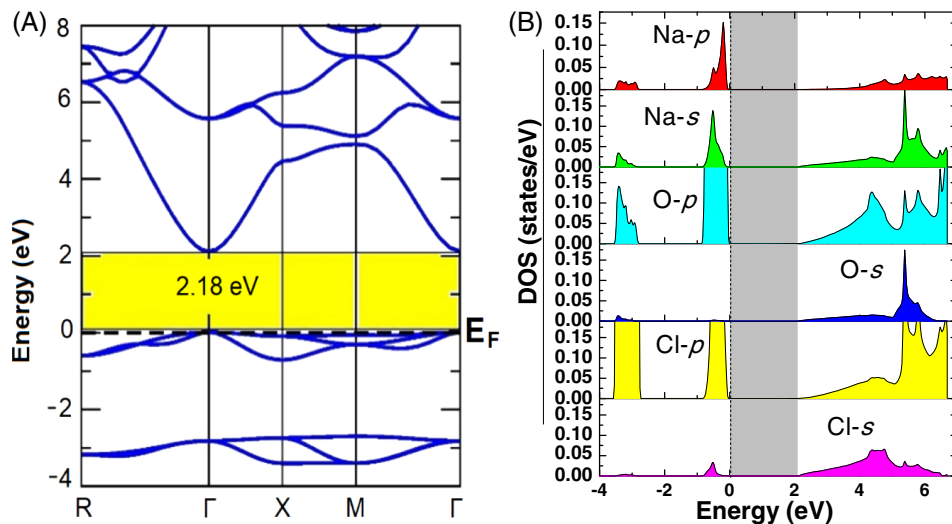


FIGURE 2 Band structure and partial density of states (pDOS) at equilibrium lattice constant for (unstrained) Na_3OCl perovskite [Color figure can be viewed at wileyonlinelibrary.com]

The large size of Br and small electronegativity than Cl decides the occupation of bands at Fermi level and hence, the effective interaction also. To confirm the exact nature of energy states around the E_F (within PBE-GGA approximation), we have plotted the partial density of states (pDOS) in Figure 2B. The projected individual contribution of DOS from the different constituent atoms permits us to plan the nature of bonding, occupation, and extent of energy states in reference to total DOS. The O-s and Cl-s states span over a narrow energy range deep inside the valence band and conduction, but away from the E_F , while as the p-states of Na, O, and Cl occupy the top of valence band states. However, the mixed p- and s-state contributions of all the three atoms cannot be neglected in the conduction band. We also calculated the DOS as well as the electronic structure w.r.t. the uniform strain (10% in both positive and negative directions) as displayed in Figure 3. Bandgap seems to increase from 3.25 eV to 1.51 eV with the increase in compressive strain from (−10 to +10% of a_0). The decrease in the band gap, is accompanied by attenuation of the pseudo gap between the core levels of valence band. At the same time, this gap decreases w.r.t. expansion when compared with the ground state unstrained bandgap. Here, the unstrained DOS refers to the equilibrium structure, where the band gap is 2.18 eV. This can be attributed to the maximum occupation of p-states of Cl and O atoms around the Fermi level, while as the p and s states of Na atom cannot be neglected. With the increase in strain, the Na-s, O-p, and Cl-p states in the conduction band (CB) come closer to the Fermi level and spread across the CB to a broader area; therefore, the reduction of the band gap region occurs significantly. These results uncover the realization of weak hybridization, so Na_3OCl can be supposed to have extra ionic character. The verification of dominant ionic character is also deduced from the computed electron density plots in (110) plane as shown in Figure 4. As observed from the

figure, the Na-O bonds, Cl-Na, and Cl-O interactions are purely ionic in nature.

3.3 | Elastic properties

The study of elastic properties of solid can play a significant role in understanding the valuable information about the structural stability and the bonding characteristics.³¹ The derivation of three elastic constants (C_{11} , C_{12} , C_{13}) for a cubic crystal can be realized pictorially from Figure 5. The physical significance of C_{11} means the elasticity along the axis of unit cell, the transverse expansion resistance (C_{12}) and shear deformation resistance (C_{44}) define the elasticity in shape, which is caused by transverse strain on the structure.³²

To derive other parameters from these constants, the following equations are considered within the Voigt-Reuss-Hill procedure.^{33–35}

$$G_V = \frac{(C_{11} - C_{12} + 3C_{44})}{5} \quad (6)$$

$$G_R = \frac{(C_{11} - C_{12})}{4C_{44} + 3(C_{11} - C_{12})} \quad (7)$$

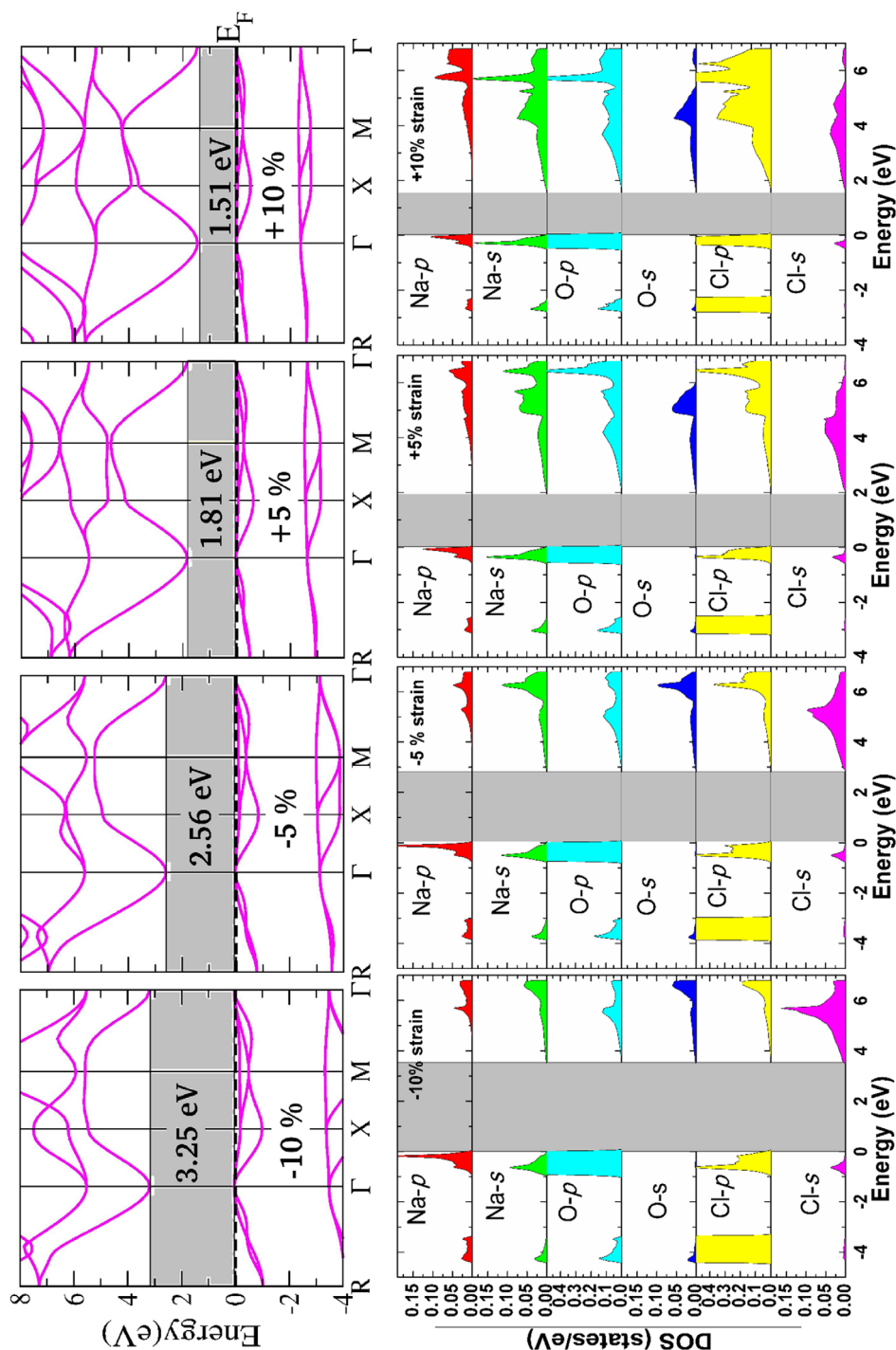
$$G = \frac{G_V + G_R}{2} \quad (8)$$

$$B = \frac{(C_{11} + 2C_{12})}{3} \quad (9)$$

$$B_V = B_G = B \quad (10)$$

$$Y = \frac{9BG}{3B + G} \quad (11)$$

FIGURE 3 Variation of band gap as a function of uniform strain. The strain is applied from -10% to $+10\%$ through zero [Color figure can be viewed at wileyonlinelibrary.com]



$$\nu = \frac{3B - Y}{6B} \quad (12)$$

$$A = \frac{2C_{44}}{(C_{11} - C_{12})} \quad (13)$$

$$C'' = C_{12} - C_{44} \quad (14)$$

The calculated values of these elastic moduli and their derivatives are listed in Table 2. The knowledge of

different elastic moduli, Poisson's ratios, and anisotropy factors is needed for possible use of the material in engineering and industrial applications, as strong materials are always preferred over weak ones. Physically, the shear modulus gives information about shear stiffness of a material. The shear modulus can also be used as an indicator of resistance to plastic deformation. It can be seen from the Table 2, that the Bulk modulus of Na_3OCl is smaller than the previously reported Na_3OBr (58.6 GPa) oxide, showing that it has a low resistance

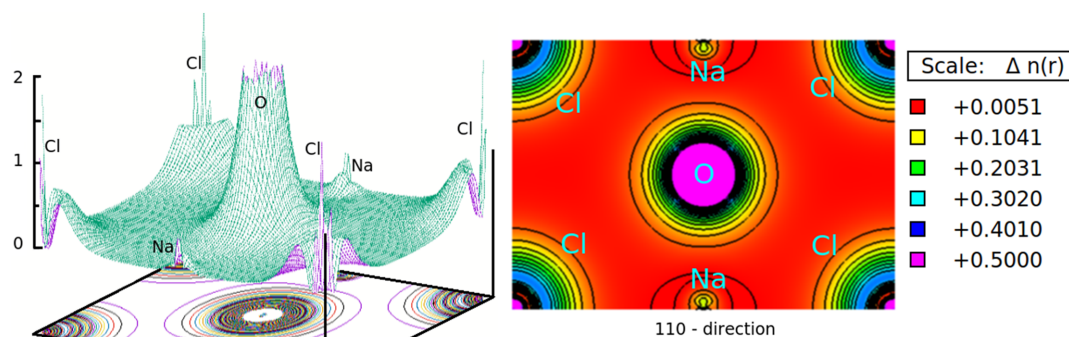


FIGURE 4 Calculated electronic charge densities (in $\text{e}\text{\AA}^{-3}$) in (110) plane at equilibrium lattice constant [Color figure can be viewed at wileyonlinelibrary.com]

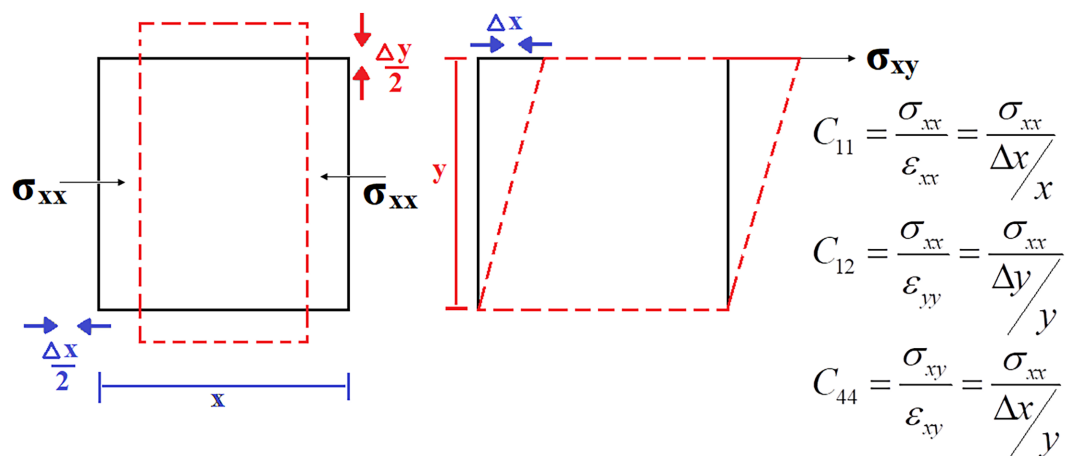


FIGURE 5 Representation of cubic elastic constants and their derivation from stress and strain relations [Color figure can be viewed at wileyonlinelibrary.com]

TABLE 2 Calculated values of elastic constants (C_{11} , C_{12} , and C_{44} in GPa), Cauchy Pressure C'' bulk modulus (B in GPa), Young's modulus (Y in GPa), shear modulus (G in GPa), Pugh's (B/G) ratio and Anisotropy factor (A) and Poisson's ratio (ν) for the Na_3OCl compound

Compound	C_{11}	C_{12}	C_{44}	C''	B	G	Y	B/G	A	ν
Na_3OCl	75.31	12.53	24.23	-11.7	33.45	26.87	63.59	1.24	0.77	0.18

towards the volumetric change. The higher the Young's modulus, the higher will be the stiffness of a material. The calculated large value of Young's moduli than bulk indicates the resistive behavior of the present material towards external uniaxial compressive forces. Thus, Na_3OCl presents greater resistance to plastic deformation as demonstrated by the shear moduli also. The Zener anisotropy for Na_3OCl is less than unity ($A = 0.77$); consequently, the material is anisotropic in nature and will have different characteristic properties (like optical and mechanical) in different crystallographic directions. Another parameter called the Poisson's ratio (ν) can be used to indicate the nature of bonding forces present in a solid. For materials with noncentral bonds $\nu < 0.25$;

while as the solids exhibiting central forces between the constituents, its value must lie in the range from 0.25 to 0.50.³⁶ In our calculations, the Poisson's ratio for Na_3OCl is 0.18 suggesting that the noncentral forces are present. According to Pugh's criterion, the material is ductile if $B/G > 1.75$, otherwise brittle. Our calculated B/G ratio for Na_3OCl is less than 1.75, classifying this compound as brittle.³⁷ According to our knowledge, no previous data on the elastic properties of Na_3OCl exists. We believe that our work may be helpful in providing reference information for future studies.

Also, the thermodynamic parameters evaluated from elastic constants are Gruneisen parameter (γ), melting temperature (T_m) and Debye temperature (θ_D).^{38,39}

TABLE 3 Calculated values of Gruneisen parameter (γ), average sound velocity (v_m) compressional velocity (v_l), shear sound velocity (v_s), Debye temperature (θ_D), melting temperature (T_m) for the compound Na_3OCl

Parameter	γ	v_l (m/s)	v_s (m/s)	v_m (m/s)	θ_D (K)	T_m (K)	Syn. temp.
Na_3OCl	1.58	2047.00	4640.09	2800.28	382.27	998.15 ± 300	873 K^{17}
Na_3OBr	0.87^{15}	—	—	—	343.60^{15}	$963.81,^{15} 528.15^{40}$	723 K^{11}

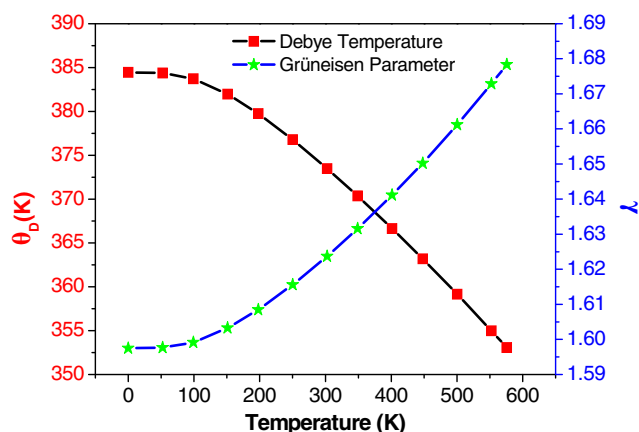


FIGURE 6 Variation of Gruneisen parameter (γ) and Debye temperature (θ_D) as a function of temperature for Na_3OCl [Color figure can be viewed at wileyonlinelibrary.com]

$$\gamma = \frac{3(1 + \nu)}{2(2 - 3\nu)} \quad (15)$$

Here the symbols have their usual meanings. Debye temperature (θ_D) can be written in terms of average sound velocity as:

$$\theta_D = \left(\frac{\hbar}{k} \right) \left[\frac{3n}{4\pi} \left(\frac{\rho N_A}{M} \right) \right]^{1/3} V_m \quad (16)$$

where v_m is the average sound velocity in terms of compressional (v_l) and shear (v_s) sound velocities as defined below:

$$V_s = \sqrt{G/\rho} \quad (17)$$

$$V_l = \sqrt{3B + 4G/3\rho} \quad (18)$$

$$V_m = \left[\frac{1}{3} \right]^{-1/3} \left[\frac{2}{V_s^3} + \frac{1}{V_l^3} \right]^{-1/3} \quad (19)$$

$$T_m(K) = [553(K) + (5.911)c_{11}] \text{ GPa} \pm 300 \text{ K} \quad (20)$$

The obtained results are shown in Table 3. It is found that the Debye temperature of Na_3OCl is 382.27 K ,¹⁶

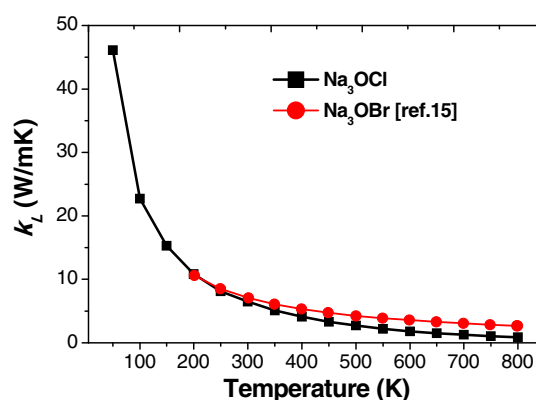


FIGURE 7 Lattice thermal conductivity (k_L) of Na_3OCl compound as a function of temperature calculated by Slack's model. The data for Na_3OBr is taken from ref. [15] [Color figure can be viewed at wileyonlinelibrary.com]

which is greater than Na_3OBr and lower than the synthesizing temperature 723 K .¹⁷ The observed value of T_m is $998.15 \pm 300 \text{ K}$, which is greater than that of previously reported Na_3OBr ($963.81 \pm 300 \text{ K}$).¹⁵

The temperature dependence of Gruneisen parameter (γ) and Debye temperature (θ_D) has been carried by the quasi-harmonic Debye model.²⁴ The possible interaction of phonon frequencies with the crystal volume is premediated by γ and can help in understanding the thermo-elastic response of a compound. It determines the vibrational frequency change in a lattice w.r.t. the applied temperature gradient. Gruneisen parameter variation (Figure 6) along the temperature grid of 0 K – 700 K shows a constant increase, signifying the phonon involvement in the lattice part of thermal conductivity in this material. Likewise, the Debye temperature (being associated to the elastic constants, melting temperature, specific heat and many other properties of a solid) is also reported in Figure 6. Within the harmonic approximation, Debye temperature displays a linear decrease w.r.t. temperature gradient and the θ_D (at zero pressure) equals 384.45 K , which is in consistence with the data calculated from the elastic constants.

Also, the lattice thermal conductivity κ_L is calculated using the famous Slack's equation as given below^{41,42} and it describes the presence of anharmonic effects in a material. Since, this method is feasible at higher temperatures where phonon contributions are maximum, so to fit this criterion here at low temperatures, we assume that the

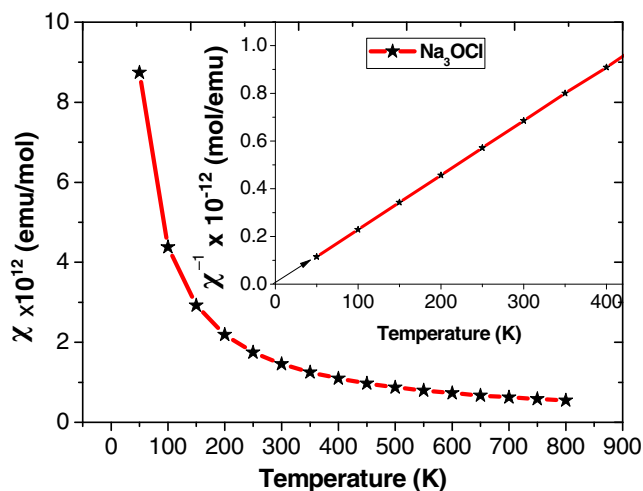


FIGURE 8 Variation of susceptibility and the inverse against temperature for Na_3OCl [Color figure can be viewed at [wileyonlinelibrary.com](#)]

onset of phonon vibrations is negligible below the much larger Debye temperature (382 K).

$$\kappa_L = \frac{A \theta_D^3 V^{1/3} m}{\gamma^2 n^{2/3} T} \quad (21)$$

where A is a collection of physical constants, calculated as follows⁴³;

$$A = \frac{2.43 \times 10^{-8}}{1 - 0.514/\gamma + 0.228/\gamma^2} \quad (22)$$

$A = 3.19 \times 10^{-8}$, θ_D is the Debye temperature, γ is Grüneisen parameter, V is the volume per atom, n is the number of atoms in the primitive unit cell, m is the average mass of all the atoms in the crystal. Lattice thermal conductivity (κ_L) from Figure 7 exponentially decreases with the increasing temperature. Its value at room temperature (6.48 W/mK) is comparable to Na_3OBr (7.30 W/mK).¹⁵ This clearly indicates the less interactive phonons below θ_D , because the phonon modes are not significant or active below this temperature and their contribution in thermal conductivity is negligible.

3.4 | Magnetic properties

In general, the magnetism of a material can be fundamentally described by the interplay of its constituent atomic spin degrees of freedom. This validates the spin magnetic moment, which thereby arranges itself in a definite order; resulting in ferromagnetic, paramagnetic, antiferromagnetic, ferrimagnetic interaction among the

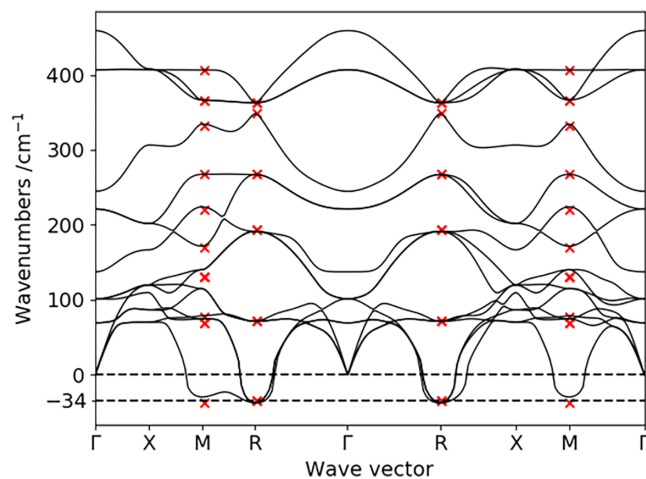


FIGURE 9 The phonon dispersion of Na_3OCl . Red crosses denote the phonon frequencies separately calculated at specific q-points, to verify the interpolation procedure [Color figure can be viewed at [wileyonlinelibrary.com](#)]

constituent atoms. In the present material, all the three atoms via Na, O, and Cl are paramagnetic, and thus they interact paramagnetically. This is supported by the susceptibility data as well, which is plotted below.

The post-DFT treatment as stated in section 2, was used to calculate the Weiss constant of this material accompanied by the variation of susceptibility and the inverse of susceptibility against temperature as shown in Figure 8. Since, for paramagnetic materials, the susceptibility follows the Curie-Weiss law; $\chi = C/(T - T_0)$.^{44,45} Here C is a material-specific Curie constant, T is temperature in Kelvin and T_0 defines the intermolecular magnetic interactions, also known as Weiss constant. $T_0 = 0$ for paramagnets and this is observed for the present material from the inverse of the magnetic susceptibility plot $1/\chi$ vs T , which passes through the origin at 0 K. However, in a material, $T_0 > 0$ or $T_0 < 0$ defines the ferromagnetic and antiferromagnetic interactions, respectively. The observed plot between magnetic susceptibility (χ) and temperature T , displays an exponential decrease in magnetic susceptibility against temperature. This happens due to the destruction of alignment in magnetic moments via thermal agitation. The maximum of susceptibility is observed to be equal to $\sim 9 \times 10^{12}$ (emu/mol) at 50 K.

3.5 | Phonon properties

The phonon dispersion as displayed in Figure 9, was computed via Fourier-interpolation from the dynamic matrix. Due to the presence of negative frequencies, the interpolation procedure was verified by recalculation of the phonon frequencies at the q-points in question (M and R). The three atoms in the unit cell of Na_3OCl give rise to three acoustical

and 12 optical modes constituting a total of 15 phonon branches. This dynamical instability displayed in Figure 9, is established by the presence of imaginary frequencies at M and R points of symmetry and the same is attributed to the antiferrodistortion.⁴⁶ The octahedral (ONa_6) rotation, due to the motion of sodium ions in these modes leads to the stress-induced phase change resulting in a spontaneous strain. Therefore, the crystal energy can be lowered through octahedral tilts as suggested by the unstable modes which thereby generate the tilted structures. These unstable modes have been linked to the Na ions only.¹⁶ Seeing how the existence of the structure is well-established experimentally¹⁷ from single-crystal diffraction, it is supposed that the structure might display a structural-phase transition.¹⁸ These results match with the previously studied instabilities mentioned in refs. [18, 46] and are thus reliable also. For cubic perovskite stability with respect to rotational instabilities of the Na_6O octahedra, one possible reason may be the Goldschmidt tolerance factor rule.⁴⁷ Generally, a cubic structure is preferred for a tolerance factor, defined as $t = (R_A + R_X) / \sqrt{2}(R_B + R_X)$,⁴⁸ between 0.9 and 1. But, the tolerance factor for Na_3OCl is 0.86. Substitution of Cl with a larger anion may dynamically stabilize the cubic perovskite with respect to Na_6O octahedral rotations. For example, Br anion alloyed in Na_3OBr sublattice results in a higher tolerance factor of 0.9 and exhibits no rotational instabilities. Therefore, future research work needs to be focused on the determination of the nature of phase transition as well as the phonon instability in this material.

4 | CONCLUSION

We have systematically performed the electronic structure, thermal, elastic, and magnetic calculations of the inverse perovskite Na_3OCl using DFT. The lattice constants and bond lengths accomplished by PBE-GGA are in reasonable agreement with experimental data. Also, this material furnishes the semiconductor type electronic structure with a direct energy band gap of 2.18 eV. The increase in band gap is observed with the increase in lattice constant and vice-versa. Furthermore, according to post-DFT calculations, this compound is reported to follow the Curie-Weiss law and is thus categorized as a paramagnetic large bandgap semiconductor. Debye temperature of Na_3OCl is found to be 382.27 K. The lattice thermal conductivity is also found to be very small at room temperature and decreases exponentially w.r.t. higher temperatures. We also found the unstable phonon modes at the M and R points like that of the literature, for the cubic phase. This instability can have its origin in the small ionic radii of Cl, which thereby decreases the tolerance factor and hence destabilizes the cubic structure.

ACKNOWLEDGEMENTS

A.L. wants to acknowledge the “Research Center of Female Scientific and Medical Colleges,” Deanship of Scientific Research, King Saud University, for the financial support. The authors also acknowledge Dr M. Mangir Murshed, Institute of Inorganic Chemistry and Crystallography, University of Bremen, Bremen, Germany, for useful discussion on phonon calculations. M. Gogolin thank the Zentrale Forschungsförderung (ZF) of the University of Bremen for providing financial support. The authors thank the North-German Supercomputing Alliance (HLRN) for the HPC-resources that have contributed to the calculation of the presented phonon results.

ORCID

Shakeel Ahmad Khandy  <https://orcid.org/0000-0002-8188-5132>

REFERENCES

1. Lotsch BV. New Light on an Old Story: Perovskites Go Solar. *Angew Chem Int Ed.* 2014;53:635.
2. Han Y, Khenata R, Yang T, Wang X. Prediction of robust multiple Dirac-cones in newly designed perovskite phase AgBO_3 from first-principles. *Results Phys.* 2019;13:102301.
3. Khandy SA, Islam I, Gupta DC, Khenata R, Laref A, Rubab S. DFT understandings of structural properties, mechanical stability and thermodynamic properties of BaCfO_3 perovskite. *Mater Res Express.* 2018;5(10):105702.
4. Targhi FF, Jalili YS, Kanjouri F. MAPbI_3 and FAPbI_3 perovskites as solar cells: Case study on structural, electrical and optical properties. *Results Phys.* 2018;10:616.
5. M. Musa Saad HE, Elhag A. DFT study on the crystal, electronic and magnetic structures of tantalum based double perovskite oxides Ba_2MTaO_6 ($\text{M}=\text{Cr, Mn, Fe}$) via GGA and GGA+U. *Results Phys.* 2018;9:793.
6. Wang WG, Li XY, Liu T, Hao GL. The effect of dual substitution of Na and Al on ionic conductivity of $\text{Na}_{0.5}\text{Bi}_{0.5}\text{TiO}_3$ ceramics. *Results Phys.* 2018;11:422.
7. Ng SW, Lim KP, Halim SA, Jumiah H. Grain size effect on the electrical and magneto-transport properties of nanosized $\text{Pr}_{0.67}\text{Sr}_{0.33}\text{MnO}_3$. *Results Phys.* 2018;9:1192.
8. Chi EO, Kim WS, Hur NH. Nearly zero temperature coefficient of resistivity in antiperovskite compound CuNMn_3 . *Solid State Commun.* 2001;120:307.
9. Mochizuki Y, Kumagai Y, Akamatsu H, Oba F. Polar metallic behavior of strained antiperovskites ACNi_3 ($\text{A}=\text{Mg, Zn, and Cd}$) from first principles. *Phys. Rev Materials.* 2018;2:125004.
10. Singh HK, Zhang Z, Opahle I, Ohmer D, Yao Y, Zhang H. High-Throughput Screening of Magnetic Antiperovskites. *Chem. Mater.* 2018;30(20):6983.
11. Wang Y, Wang Q, Liu Z, Zhou Z, Li S, Zhu J, Zou R, Wang Y, Lin J, Zhao Y. Enhanced ionic conductivity with $\text{Li}_7\text{O}_2\text{Br}_3$ phase in Li_3OBr anti-perovskite solid electrolyte. *J. Power Sources.* 2015;293:735.
12. Tong P, Louca D, King G, Llobet A, Lin JC, Sun YP. Size effects on negative thermal expansion in cubic ScF_3 . *Appl. Phys. Lett.* 2013;102:041908.

13. Zhao Y, Daemen LL. Superionic Conductivity in Lithium-Rich Anti-Perovskites. *J. Am. Chem. Soc.* 2012;134:15042.
14. Wang Y, Wen T, Park C, Benson CK, Pravica M, Yang W, Zhao Y. High pressure high temperature devitrification of Fe₇₈B₁₃Si₉ metallic glass with simultaneous x-ray structural characterization. *J. Appl. Phys.* 2016;119:025901.
15. Lv ZL, Cui HL, Wang H, Li XH, Ji GF. Electronic, elastic, lattice dynamic and thermal conductivity properties of Na₃OBr via first principles. *Phys. Status SolidiB.* 2017;254:1700089.
16. Sabrowsky H, Paszkowski K, Reddig D, Vogt P. Na₃OCl und Na₃OBr, die ersten Alkalimetallchalkogenidhalogenide. *Z. Naturforsch.* 1988;43b:238. <http://www.znaturforsch.com/ab/v43b/43b0238.pdf>
17. Hippler K, Sitta S, Vogt P, Sabrowsky H. Structure of Na₃OCl. *Acta Cryst.* 1990;C46:736.
18. Pham TL, Samad A, Kim HJ, Shina YH. Computational predictions of stable phase for antiperovskite Na₃OCl via tilting of Na₆O octahedra. *J. Applied Physics.* 2018;124:164106.
19. Blaha P, Schwarz K, Sorantin P, Trickey SB. Full-potential, linearized augmented plane wave programs for crystalline systems. *Comput. Phys. Commun.* 1990;59:399.
20. Blaha P, Schwarz K, Madsen GKH, Kvasnicka D, Luitz J. WIEN2k, An Augmented Plane Wave Plus Local Orbitals Program for Calculating Crystal Properties, Vienna University of Technology, Vienna, (2001). http://susi.theochem.tuwien.ac.at/reg_user/textbooks/usersguide.pdf. 2012.
21. Perdew JP, Burke K, Ernzerhof M. Generalized Gradient Approximation Made Simple. *Phys. Rev. Lett.* 1996;77:3865.
22. Jamal M. Cubic-elastic, http://www.WIEN2k.at/reg_user/unsupported/cubic-elast/, (2012). http://susi.theochem.tuwien.ac.at/reg_user/unsupported/cubic-elast/guide-Cubic.pdf
23. Khandy SA, Gupta DC. Investigation of structural, magneto-electronic, and thermoelectric response of ductile SnAlO₃ from high-throughput DFT calculations. *Int. J. Quant. Chem.* 2017;117:e25351. <https://doi.org/10.1002/qua.25351>
24. Blanco MA, Francisco E, Luana V. Gibbs2: A new version of the quasi-harmonic model code. I. Robust treatment of the static data. *Comput. Phys. Commun.* 2004;158:57.
25. Khandy SA, Chai JD, Magn J. Novel half-metallic L21 structured full-Heusler compound for promising spintronic applications: A DFT-based computer simulation. *Magn. Mater.* 2019;487:165289.
26. Madsen GKH, Singh DJ. BoltzTraP. A code for calculating band-structure dependent quantities. *Comput. Phys. Commun.* 2006;175(1):67.
27. Khandy SA, Islam I, Gupta DC, Laref A. Predicting the electronic structure, magnetism, and transport properties of new Co-based Heusler alloys. *Int. J. Energy Research.* 2018;42(13):4221.
28. Giannozzi P, et al. Advanced capabilities for materials modeling with Quantum ESPRESSO. *J. Phys. Condens. Matter.* 2017;29:465901.
29. Giannozzi P, et al. QUANTUM ESPRESSO: a modular and open-source software project for quantum simulations of materials. *J. Phys. Condens. Matter.* 2009;21:395502.
30. Perdew JP, Ruzsinszky A, Csonka GI, et al. Restoring the density-gradient expansion for exchange in solids and surfaces. *Phys. Rev. Lett.* 2008;100:136406.
31. Ravindran P, Fast L, Korzhavyi PA, Johansson B. Density functional theory for calculation of elastic properties of orthorhombic crystals: Application to TiSi₂. *J. Applied Phys.* 1998;84(9):4891.
32. Voigt W. Lehrbuch der Kristallphysik (B. B. Teubner, Leipzig, 1928), p. 739.
33. Reuss A, Angew Z. Berechnung der Fließgrenze von Mischkristallen auf Grund der Plastizitätsbedingung für Einkristalle. *Math. Mech.* 1929;9:49.
34. Hill R. The Elastic Behaviour of a Crystalline Aggregate. *Proc. Phys. Soc (London).* 1952;65:349.
35. Khandy SA, Islam I, Gupta DC, Laref A. Electronic structure, mechanical and thermodynamic properties of BaPaO₃ under pressure. *J. Mol. Model.* 2018;24:131.
36. Kaur K, Kumar R. High temperature thermoelectric performance of p-type TaRhSn half-Heusler compound: A computational assessment. *Ceramics International.* 2017;43:15160.
37. Schreiber E, Anderson OL, Soga N. "Elastic Constants, and Their Measurements" McGraw-Hill, New York, (1973).
38. Khandy SA, Gupta D. Investigation of the transport, structural and mechanical properties of half-metallic REMnO₃ (RE = Ce and Pr) ferromagnets. *RSC. Adv.* 2016;6:97641.
39. Khandy SA, Islam I, Ganai ZS, Gupta DC, Parrey KA. High-Temperature and High-Pressure Study of Electronic and Thermal Properties of PbTaO₃ and SnAlO₃ Metal Perovskites by Density Functional Theory Calculations. *J. Electron. Mater.* 2018;47(1):436.
40. Nguyen H, Hy S, Wu E. Computational predictions of stable phase for antiperovskite Na₃OCl via tilting of Na₆O octahedra. *J. Electrochem. Soc.* 2016;163:A2165.
41. Hong AJ, Li L, He JJ, et al. Full-scale computation for all the thermoelectric property parameters of half-Heusler compounds. *Sci. Rep.* 2016;6:22778.
42. Khandy SA, Gupta DC, Magn J. Electronic structure, magnetism and thermoelectric properties of double perovskite Sr₂HoNbO₆. *Magn. Mater.* 2018;458:176.
43. Morelli DT, Slack GA. in High Thermal Conductivity Materials (eds S.L. Shinde & J.S. Goela) (Springer, 2006). High Lattice Thermal Conductivity Solids. https://link.springer.com/chapter/10.1007/0-387-25100-6_2
44. Blundell S. "Magnetism in Condensed Matter" Oxford University Press, New York, USA, (2001). <https://global.oup.com/ukhe/product/magnetism-in-condensed-matter-9780198505914?cc=tw&lang=en&>
45. Khandy SA, Gupta D. Structural, elastic and thermo-electronic properties of paramagnetic perovskite PbTaO₃. *RSC. Adv.* 2016;6:48009.
46. Zinenko VI, Zamkova NG. Lattice dynamics of antiperovskite structure compounds a₃ox (a=na, k; x=ci, br). *Ferroelectrics.* 2002;265:23.
47. Goldschmidt V. Die Gesetze der Krystallochemie. *Naturwiss.* 1926;14:477.
48. Min-Hua Chen, Alexandra Emly, Anton Van der. Anharmonicity and phase stability of antiperovskite Li₃OCl. *Ven Phys. Rev. B.* 2015;91:214306.

How to cite this article: Khandy SA, Islam I, Laref A, Gogolin M, Hafiz AK, Siddiqui AM. Electronic structure, thermomechanical and phonon properties of inverse perovskite oxide (Na₃OCl): An ab initio study. *Int J Energy Res.* 2020;44:2594–2603. <https://doi.org/10.1002/er.4982>